Nanoscale

Accepted Manuscript

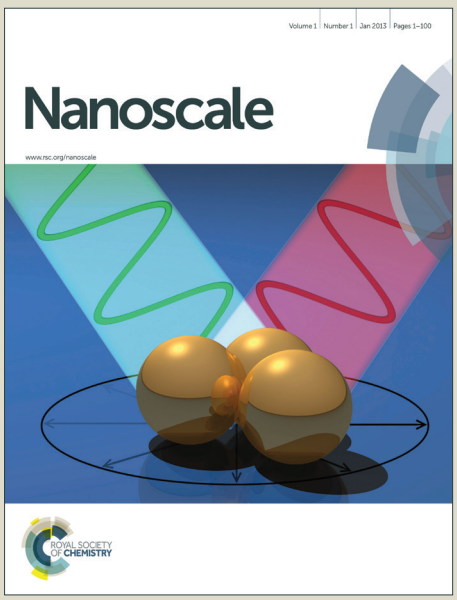

ROYAL SOCIETY OF CHEMISTRY

www.rsc.org/nanoscale

Nanoscale

RSCPublishing

ARTICLE

Strain-rate stiffening of cortical bone: observations and implications from nanoindentation experiments

Cite this: DOI: 10.1039/xoxxoooooox

Received ooth January 2012,
Accepted ooth January 2012

DOI: 10.1039/xoxxoooooox

www.rsc.org/

Noriko Maruyama[1], *Yo Shibata[2], Wurihan[2], Michael V. Swain[3,4], Yu Kataoka[2], Yuichi Takiguchi[2], Atsushi Yamada[5], Koutaro Maki[1], and Takashi Miyazaki[2]

[1]Department of Orthodontics, Showa University School of Dentistry, 1-5-8 Hatanodai, Shinagawa-ku, Tokyo 142-8555, Japan;[2]Department of Conservative Dentistry, Division of Biomaterials and Engineering, Showa University School of Dentistry, 1-5-8 Hatanodai, Shinagawa-ku, Tokyo 142-8555, Japan; [3]Biomaterials Unit, Sydney Dental Hospital, University of Sydney, Sydney, NSW, Australia; [4]Sir John Walsh Research Institute, Faculty of Dentistry, University of Otago, Dunedin 9054, New Zealand, [5]Department of Biochemistry, Showa University School of Dentistry, 1-5-8 Hatanodai, Shinagawa-ku, Tokyo 142-8555, Japan

Abstract: While bone mineralization is considered to be responsible for its stiffness, bone durability partially associated with the time-dependent viscoelasticity of matrix proteins is still poorly elucidated. Here we demonstrate a novel mechanism of highly mineralized bone durability almost independent of inherent viscoelastic behaviour along with a protocol for measuring the mechanical properties of mineralized tissues. Strain-rate nanoindentation tests showed substantial stiffening for highly mineralized calvarial bone, whereas substantial creep or stress relaxation was observed during constant load- or displacement tests, respectively. Based on the lower viscoelasticity of highly mineralized structure, such large time-dependent response appears to be associated with nanoscale dimensional recovery, rather than viscoelastic behaviour, implying the inverse namely strain-rate dependent dilatant behaviour. This dilatant expansion increased the indenter penetration resistance into the surface, enhancing instantaneous stiffness. The associated stiffening and higher effective elastic modulus was highly strain-rate dependent and more readily observed in more highly mineralized tissue such as calvarial bone. Such strain-rate stiffening and consequent dimensional recovery may be vital responses of bone tissues against excessive deformation to maintain tissue integrity. **Keywords:** Bone, Mineralization, Nanoindentation, Dynamic mechanical analysis, Nanomechanical properties, Elasticity, Viscoelasticity

Correspondence to: Y. Shibata (e-mail: yookun@dent.showa-u.ac.jp)

Introduction

The remarkable stiffness and durability are mandatory requirements for bone mechanical properties despite the fact that an enhanced stiffness of highly mineralized bone is theoretically accompanied with brittle like behaviour. Although the energy dissipation associated with the time-dependent viscoelasticity of matrix proteins is known and is thought to be partially responsible for the remarkable durability of bone [1-3], the underlying mechanism is still poorly understood and has not been fully duplicated by artificial biopolymers or composites.

Strain-stiffening has been proposed as a vital response mechanism of soft biological tissue against excessive deformation to maintain tissue integrity [4-8]. When soft biological tissues, such as blood vessels, mesentery tissue, lung parenchyma, and semi-flexible fibrin, among others[4, 6], are subjected to large strain, they resist deformation through increases in material stiffness. This occurs because of their specialized hierarchical structure in combination with fluid and proteins that impart complex non-linear viscoelastic and/or poroelastic responses. It is generally assumed that even mineralized hard tissues, such as bone and teeth, follow to this rule[9, 10].

Bone is an inhomogeneous, anisotropic material with complex, multiscale structural variations[11]. Thus, experiments at the bulk scale using universal mechanical testing machine are not applicable for localised precision mechanical testing of bone-like structures. Alternatively, nanoscale mechanical testing technology such as nanoindentation enables measurements of local materials properties in heterogeneous structures so that mechanical properties of bone could be measurable at the micron level[12]. Moreover, nanoindentation systems currently enable both high placement precision and the ability to capture material responses over a wide range of strain-rates by utilizing dynamic force and displacement amplitudes with increasing frequency[11, 13]. Additionally, quasi-static constant loading achieves extremely low strain-rates[14], while constant displacement theoretically approaches zero strain-rate[15]. As such, the strain-rate dependent moduli of a material may be described by a series of nanoindentation experiments. Such indentation experiments invariably simultaneously capture both elastic and viscoelastic properties, and thus the calculated elastic modulus (storage modulus) for each test must be corrected by subtracting the viscoelastic response (loss modulus) [11, 13-16]. In the present study, we discuss the strain-rate dependent moduli of cortical region mouse bone obtained by quasi-static and dynamic nanoindentation tests. The underlying concept of this bone nanoindentation study was to evaluate strain-rate dependent mechanical responses of relatively higher or lower mineralized cortical bone within an individual mouse. In this context, our findings minimize the consequences of bone structural heterogeneity anticipated in each region of interest.

Results

Based on Raman spectroscopy of the mineral-to-organic matrix ratio, the ossification of the calvaria and tibia was still considered to be immature at 2 wks of age (Supplemental Fig. 1). Histological observations of cortical regions are shown in Fig. 1. Bone lacunae with varying range from 5- 20 μm were observed. Indentation impression size needs to be sufficiently small to avoid the influence of adjacent structures.

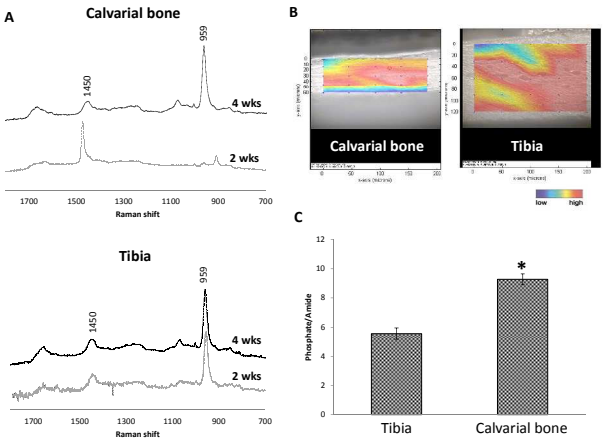

Supplemental Fig. 1
Raman spectra of calvarial bone and tibia of ddY mice at 2 and 4 wks old (A). The intensities of υ1 phosphate/amide III of calvaial bone and tibia from 4 wks old mice were visualized (B) and quantified (C). A p-value of less than 0.05 was considered significant (*).

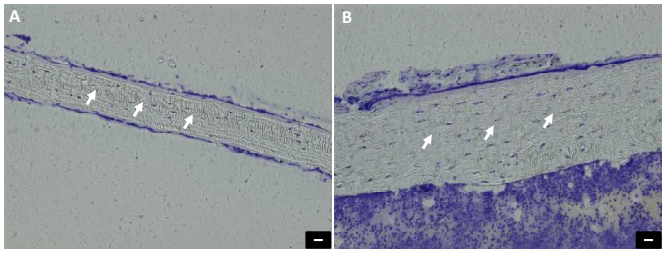

Fig. 1
Representative light microscope images of calvarial cortical bone (A) and tibia (B) of ddY mice 4 wks old (scale bars = 20 μm) Nanoindentation sites are marked with arrows.

The elastic moduli of all bone samples at 4 wks of age were constant between 50–200 nm indenter contact depths (Fig. 2) and hence all subsequent tests were performed on bone samples at 4 wks.
The mineral-to-organic matrix ratio and constant elastic moduli obtained by preliminary loading/partial unloading tests of calvarial bone were significantly higher ($p < 0.05$) than for tibia. This agrees with theoretical considerations that the elastic modulus of mineralized tissue is entirely associated with bone mass or mineral density[17-19].

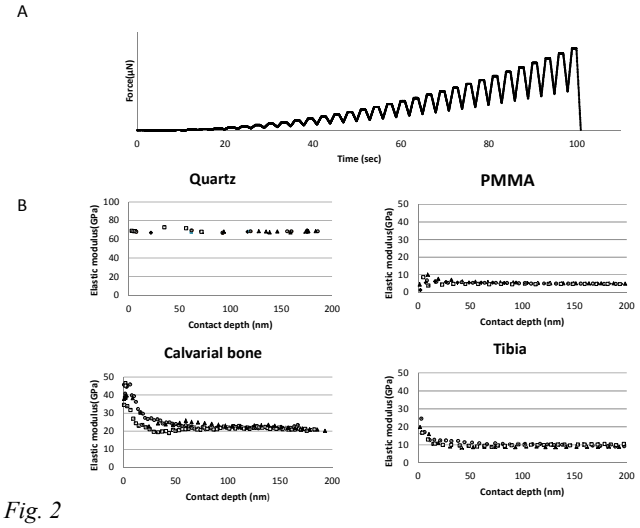

Fig. 2
A representative load-time indentation response used to quantify depth dependent loading/partial unloading response (A). The effective measurement range of the nanoindentation tests for the samples (B). Material homogeneity of the specimens was confirmed by the observation of near constant elastic moduli within the 50-200 nm penetration depth range.

The corrected elastic moduli of each nanoindentation test were not statistically different ($p > 0.05$) except for calvarial bone (Fig. 3).

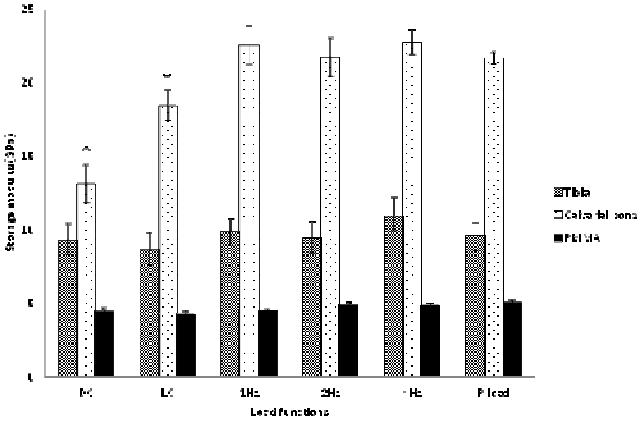

Fig.3
Corrected elastic modulus (storage modulus) of the different materials from indentation tests using loading/partial unloading (P-load), load control at 0 Hz (LC; creep) and displacement-controlled (DC). The storage moduli of each nanoindentation test were equivalent ($p > 0.05$) except for calvarial bone ($p < 0.05$).*

The storage modulus of calvarial bone increased significantly ($p < 0.05$) with strain-rate. Specifically, quasi-dynamic (loading/partial unloading) or dynamic (sinusoidal) indentation tests yielded the highest moduli, while the displacement-controlled yielded the lowest.
Based on its homogeneous polymeric structure, poly(methyl methacrylate) (PMMA) generated the largest phase lag (tan δ) and creep rate to the applied stress, while those of fused quartz were lowest because its mechanical properties are almost time-independent (Fig. 4, 5A).

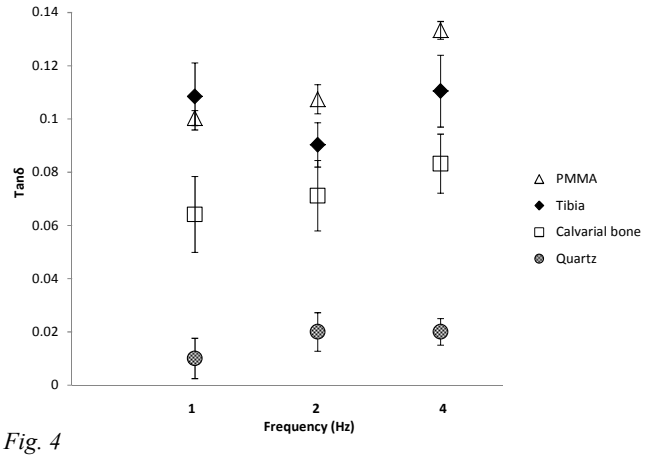

Fig. 4
Viscoelastic (tan δ) properties of different materials at 1–4 Hz.

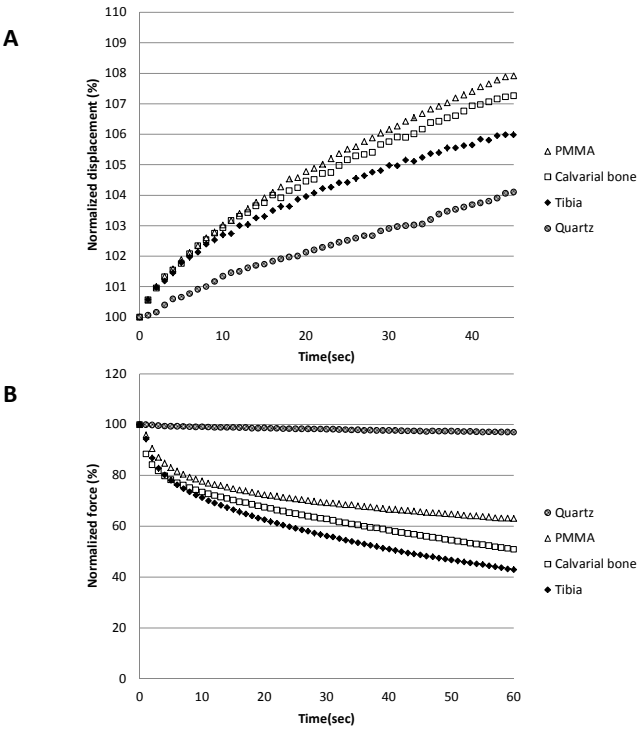

Fig. 5
Normalized time-dependent creep rate during constant load (A: average) and stress relaxation of different materials under constant displacement tests (B: average). The vertical axis of (A) reveals the increased indenter penetration as a % of the initial displacement at max load during constant loading. The vertical axis of (B) reveals the force reduction, as a % of the maximum load, during displacement-controlled indentation at the controlled contact depth. The values of at least five indentation tests were merged.

The normalized creep (Fig. 5A) and tan δ (Fig. 4) magnitudes of bone samples lay between those of PMMA and fused quartz, and the tan δ values of tibia were significantly higher ($p < 0.05$) than those of calvarial bone. The normalized creep of calvarial bone was similar to PMMA while the tan δ was significantly lower ($p < 0.05$) than tibia.

During constant strain displacement-controlled indentation testing, viscoelastic materials allow stress (load) relaxation with time because their viscous deformation results in an increase in the contact area[15, 20]. On this basis, PMMA was expected to display the largest stress relaxation due to its relatively higher viscoelastic response[21]. Nevertheless, the less viscoelastic bone samples showed greater ($p < 0.05$) stress relaxation than PMMA (Fig. 5B). Although tibia allowed faster force reduction at the onset of constant displacement, the overall stress relaxation rates of tibia and calvarial bone were not statistically different ($p > 0.05$).
The corrected contact stiffness (S_e) calculated from equation (6) for quartz, PMMA and tibia during load-controlled or displacement-controlled indentations overlapped with the linear contact stiffness obtained from the depth-dependent loading/partial loading test (Fig. 2, 6), whereas those of the S_e for calvarial bone were lower ($p < 0.05$) than the linear contact stiffness obtained from the depth-dependent loading/partial loading test (Fig. 6).

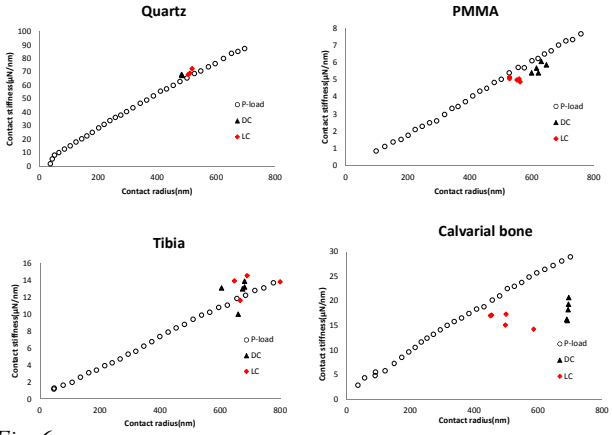

Fig. 6
Effective contact stiffness vs. contact radius obtained from loading/partial unloading (P-load) tests (the values of at least five indentation tests were merged), displacement-controlled (DC) tests and load-controlled (LC) tests for all specimens. Note the significant difference of the DC- and LC-derived data points from the linear trend of P-load tests for calvarial bone.

Discussion

Bone is a complex hierarchical tissue with different structural levels, namely cortical and trabecular bone at the macroscale, haversian osteons and lamellae at the microscale, and hydroxyapatite crystals and collagen fibres at the nanoscale [22, 23]. Using the estimated tip contact area and the constant elastic modulus of each bone sample (contact depth 50-200 nm), from the series of nanoindentation tests within this target measurement range revealed homogeneous bone nanomechanical properties. According to a simple viscoelastic Maxwell model represented by a viscous dashpot and elastic spring connected in series[24], strain-rate stiffening of viscoelastic materials is anticipated because the dashpot cannot instantaneously respond to high strain-rates, thereby resulting in less deformation and enhanced apparent stiffness.
The mineral phase affects bone stiffness, whereas the collagen matrix protein and liquid present within the tissue contributes to the viscoelastic behaviour[11, 25, 26]. Thus, the less mineralized tibia would be expected to demonstrate more viscoelastic behaviour than the more highly mineralized calvarial bone. The present data showed a greater viscoelastic tan δ in the tibia and PMMA compared with the calvarial bone. However, strain-rate stiffening was only detected in calvarial bone.
Apart from the lower intrinsic viscoelasticity of calvarial bone, the associated effective strain-rate during initial unloading, as

determined from the unloading slope of each indentation test, may be a critical parameter responsible for the observed variation in the storage moduli. At lower strain-rate, materials exhibiting time-dependent mechanical behaviour undergo greater deformation and thereby reduce contact stiffness[14]. Indeed, even though the unloading strain-rate (unloading elastic deformation/time) of calvarial bone was highest, the corrected elastic modulus in the displacement-controlled indentation tests was lowest. Given these observations, the strain-rate stiffening of calvarial bone was unlikely to be primarily associated with the viscoelastic considerations described above.

On the basis of lower tan δ associated with higher mineral content, the creep and stress relaxation observed for calvarial bone is not fully explained by viscoelastic behaviour. Rather, such contact stiffness decreases suggest a reduction in the contact area along with material surface dimensional recovery during low strain versus rapid load indentation because of the poroelastic nature of calvarial bone[27]. According to equation (1), contact stiffness (S) linearly increases with tip contact area, enabling constant elastic moduli materials to be measured regardless of the applied force to the sample surface. However, corrected contact stiffness (S_e) calculated from equ (6) for calvarial bone during load- and displacement-controlled indentations was less than linear contact stiffness obtained from depth-dependent loading/partial loading tests (Fig. 6). This implies pile-up opposing indenter penetration because of reduced fluid permeability within the bone which with time would diffuse radially and to a reduction in pile-up and diminishing contact area during constant load and displacement following rapid load indentation. Additionally, a substantial reduction appeared in displacement controlled indentation (theoretically approaches zero strain-rate) compared to those of load-controlled indentation (extremely low strain-rate) revealed a strain-rate stiffening for calvarial bone.

Bone is often considered to be a fluid saturated porous network [27]. According to poroelastic theory, strain-rate stiffening of calvarial bone could be interpreted as a dilatant response to an instantaneous increase in pore pressure (Fig. 7A). Under shear displacement, most materials have a tendency to expand in the direction perpendicular to the applied shear stress [4, 6, 28]. In the quasi-dynamic and dynamic indentation tests, substantial shear strain was generated in the bone region parallel to the indenter tip-material interface, especially during cyclic oscillations. For a dilatant material, deformation primarily occurs perpendicular to the direction of indenter surface penetration resulting in a pile-up of material around the indenter tip that can increase the contact area and the resultant instantaneous contact stiffness (Fig. 7B).

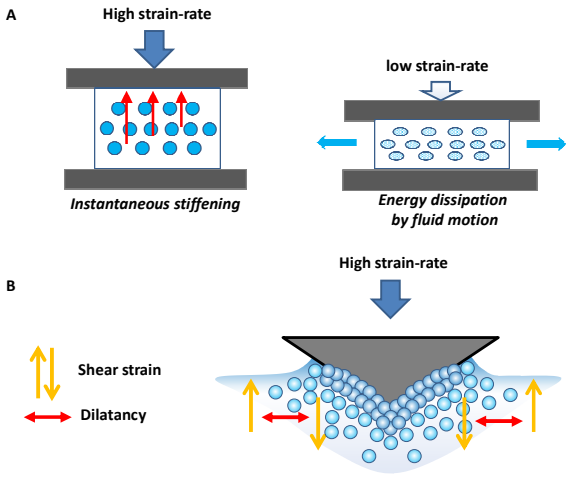

Fig. 7
Schematic illustrations of material surface dimensional recovery during constant strain (or constant load) associated with pressure induced diffusion (drainage) of pore fluid through the poroelastic material (A) and pile-up opposing indenter penetration at higher strain-rate indentation (B).

During unloading recovery, apart from the elastic recovery also proteins refolding and fluid permeability or flow back into the deformed area surrounding the impression would occur. For constant load or displacement tests, creep or force relaxation would occur due to protein unfolding and fluid diffusion displacement respectively. In the case of multi cyclic loading a quasi-dynamic and dynamic indentation condition was achieved and did not allow sufficient time for dimensional recovery and hence calvarial bone surface generated enhanced unloading stiffness. In this context, the higher collagen and fluid (porosity) content of the tibia is less able to generate sufficient resistance to instantaneous strain than calvarial bone, and the tibia behaves as a more apparent viscoelastic material, although the creep or force relaxation could also be associated with reduction in the contact area such as allowed in calvarial bone.

The observed enhanced stiffness against strain-rates and consequent dimensional recovery of mineralized tissues are assumed to be the consequence of physical contacts between each apatite crystal, the deformation of the adhering proteins[2] and fluid permeability. A structural motif of mineralized tissues, including bone, dentin, and tendon, typically consists of staggered arrays of stiff mineral embedded in much softer matrix proteins, and is often used to interpret the non-linear stiffness of such tissues[29]. One limitation of this motif is that all mechanical simulations have been carried out assuming "perfect bonding" between mineral and matrix proteins or synthetic polymers and an absence of fluid, making it difficult to determine specific bone mechanical properties, such as strain-rate stiffening, as reported here.

According to a previous study by Shipov et al., cartilaginous tissues remain within the cortical region in an adult rat after endochondral ossification[30], whereas inter-membranous ossification of calvarial bone generates more bone mineralization. Such microstructural, histological, and associated mineral content differences between tibia and calvarial bones may result in clear differences between their viscoelastic and poroelastic mechanical properties. The major role of calvarial bone is considered to be the protection of internal soft brain-like cellular organization. Large elastic or viscoelastic deformable tissue cannot be tolerated, rather calvarial bone needs to be highly mineralized so that the tissue is harder and stiffer than other bone mineral structures. However, calvarial bone must be tough and should achieve energy dissipation despite the reduction of viscoelasticity. The durability of highly mineralized bone might be partially associated with the estimated dimensional recovery process, as the inverse of instantaneously enhanced stiffness, as well as the time-dependent viscoelasticity.

Regarding future directions of bone research, we have placed strong emphasis on the nanoindentation protocol for use in a pathological model such as genetically mutant mice. Whereas the development of new bone substitute materials may be anticipated to lie in the range of mechanical properties between natural bone and artificial materials and is more reliably investigated with the precision nano-indentation protocol advocated in this study.

Experimental

Bone specimen preparation

Four male ddY mice (Sankyo Co. Inc., Tokyo, Japan) were euthanized at 2 and 4 wks of age following an approved protocol by

the Animal Care and Use Committee of Showa University (Tokyo, Japan; ref.13080). The calvarial bones and tibiae were harvested, the surrounding soft tissue was removed, and they were stored in Hanks' balanced salt solution (Sigma, St. Louis, MO, USA) at 8°C until testing (less than 2 wks). The bones were cross-sectioned in the longitudinal direction using a cryostat (CM 3050S, LEICA, Frankfurt, Germany). For histolochemical observation, the cut surface was covered with an adhesive film (Cryofilm type IIC9, SECTION-LAB, Hiroshima, Japan) and frozen sections (10 mm) were prepared according to a method described previously[31]. The resulting sections were stained with toluidine blue and analyzed with a microscope (BZ-9000, Keyence, Osaka, Japan).The cross-sectioned calvarial bones and tibiae were embedded in a cold-cure epoxy resin (Palapress vario, Heraeus Kulzer GmbH, Hanau, Germany) for 24 hrs at room temperature. The cross-sectioned surface of calvarial bones and the diaphyseal surface of the tibiae were polished manually with silicon carbide paper (#800–1000), and then polished with 0.3–0.05 μm alumina polishing paste (Buehler, Lake Bluff, IL, USA) so that fine surfaces were generated on the cortical regions of both calvarial bones and tibiae. The samples were ultrasonically cleaned with distilled water for 10 s between each step.

Micro-Raman spectroscopy

Raman spectra of the region marked for indentation measurements were acquired using a confocal Raman microscope (RXN1, Kaiser Optical Systems Inc., Ann Arbor, MI, USA) with a 785-nm laser diode source. A 50× objective focused light on a 3 μm spot on the sample surfaces. The Raman scattered light (10 s exposure) was collected by a spectrometer with a spectral resolution of 1 cm^{-1}. From each Raman transect, a normalized mean spectrum was generated to offset the effect of a single spectrum on the arithmetic mean. These transects were imported into Matlab 12.1 (The MathWorks Inc., Natick, MA, USA), wherein the spectra were corrected for dark signals and averaged into normalized spectra. Background signals were removed from the normalized spectra using a user-defined multipoint baseline routine, and the Raman bands were curve-fit if all the band intensities were non-negative and the fit yielded an R^2 value greater than or equal to 0.99. Raman shift assignments for bone mineral and matrix were previously reported[32], and a spectroscopic parameter proportional to the mineral-to-organic-matrix ratio was used[32, 33]. The maximum height of the phosphate υ_1 band at 959 cm^{-1} was calculated and normalized to the maximum height of the CH_2 wag band at 1450 cm^{-1}. Ten mineral-to-organic matrix ratio values were generated for each sample, and a standard deviation was calculated from these 10 values. 5 x 5 point Raman maps (HoloMap™; Kaiser Optical Systems) were performed on the surface of calvarial bones and tibiae with dimension of 170 μm x 60 μm and 600 μm x 600 μm, respectively, according to the sample shape. A 50× objective focused light on a 3 μm spot on the calvarial bones, while a 10× objective focused light on a 10 μm spot on the tibiae. The magnitude of the phosphate υ_1 band at 959 cm^{-1} and the CH_2 wag band at 1450 cm^{-1} were visualized and subsequent indentations were performed on the highly mineralized portions. We confirmed that no epoxy resin had infiltrated into the selected regions of the bone samples prior to indentation testing.

Nanoindentation experiments

The samples were briefly submerged in Hanks' balanced salt solution (Sigma) prior to testing. Nanoindentation experiments were performed on the cortical regions of the bone samples using a diamond Berkovich tip on a quantitative nanomechanical test instrument (TS 70 TriboScope, Hysitron, Inc., Eden Prairie, MN, USA) interfaced with a scanning probe microscope (SPM-9700, Shimadzu, Kyoto, Japan). To minimize errors arising from surface roughness, sufficiently smooth mineralized regions were chosen with a scanning range of 50 μm × 50 μm and then 1 μm × 1 μm. The series of nanoindentation tests was also performed within a scanning range of 50 μm × 50 μm. Fused quartz was used as the standard calibration material to determine the indenter tip area function and the compliance of the instrument[34, 35]. The distance between indents was kept greater than 10 μm to avoid any influence of residual stresses from adjacent indentations. The thermal drift rate at a contact load of 3 μN was monitored for 40 s prior to indentation to correct the indentation depth data for thermal drift based on the time-mean drift rate over the latter 20 s.

The measured indentation data of each sample in the contact depth range of 20 to 200 nm were used to ensure that the pyramidal portion of the Berkovich indenter always dominated the contribution to the measured mechanical properties of the sample. The load applied to the sample was controlled using a closed-loop load-control algorithm for all quasi-static tests performed in this study. For the closed-loop load-control tests, the indenter tip was first withdrawn from the surface to a set distance (lift height) and then the re-captured sample surface was determined based on a pre-load of 3 μN. The reduced elastic modulus, *Er*, was calculated from the force–displacement curve using the standard unloading analysis procedure[34] according to Equation (1), where *S* is the contact stiffness calculated as the slope of the unloading curve at the onset of unloading and *A* is the projected area of the indenter tip as a function of the contact depth.

$$Er = \frac{S\sqrt{\pi}}{2\sqrt{A}} \quad (1)$$

Nanoindentation tests were also performed on fused quartz and polymethyl methacrylate (PMMA, TGK, Tokyo, Japan) as representative time-independent and linear viscoelastic materials, respectively.

Effective measurement range

To determine the effective range of nanoindentation depths for each sample, the elastic moduli of all samples were measured as a function of depth using the partial unloading technique[36] with a load function containing a total of 33 partial unloading cycles, each comprising a 1 s loading segment, a 1 s hold segment, and a 1 s unloading segment. Typical nanoindentation analysis is based on the assumption of isotropic elastic-plastic materials[12]. However, biological tissues often exhibit viscoelastic or time-dependent behaviours. When loading is followed by unloading without a sufficiently long hold period at the peak load, displacement continues to increase during the initial portion of the unloading phase, resulting in an overestimation of the actual elastic contact stiffness of the sample. This phenomenon can result in a negative slope in the initial unloading region, making it impossible to quantify the elastic modulus accurately. For the current tests, each loading portion was followed by a 1 s hold period to minimize the effect of creep on the unloading stiffness. The elastic moduli of biological tissues may also vary as a function of the unloading strain-rate[12]. Material homogeneity of the specimens was confirmed by the observation of near constant elastic moduli within the effective measurement area (Fig. 2). The following dynamic- or quasi-static nanoindentation tests were performed within the range of constant elastic moduli on each sample.

Dynamic nanoindentation test

Force-displacement curves with a loading/partial unloading portion were recorded using a loading rate of 50 μN/s to a maximum load of 500 μN. The loading portion was followed by a 10 s hold and partial unloading curve to 250 μN. Subsequent reloading to the maximum

load of 500 μN was undertaken to enable nearly pure elastic deformation. The latter loading portion was followed by a 20 s hold, and then five sinusoidal oscillation indentations were superimposed on the force-displacement curve of the loading/partial unloading tests. The applied amplitudes for the sinusoidal oscillations were 50 μN at frequencies of 1, 2, and 4 Hz. The former triangular oscillations mimicked the following sinusoidal indentation profiles with equal amplitudes and instantaneous holding times. The amplitudes of the triangular oscillations enabled constant dynamic strain prior to the sinusoidal frequency so that the delayed stress-strain responses obtained from the sinusoidal oscillations that followed were stable (Supplemental Fig. 2).

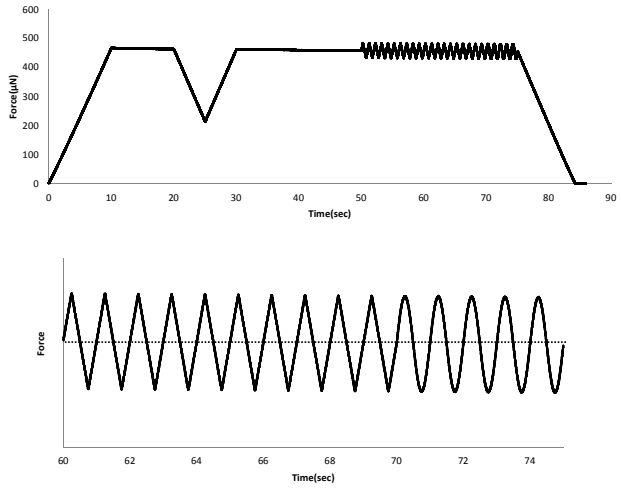

Supplemental Fig. 2
A representative load function of the dynamic indentation tests. The lower panel indicates the superimposed oscillations and sinusoidal indentations within the dynamic indentation tests.

The above loading procedures were determined by considering effective area functions and measurement ranges according to depth-dependent loading/partial unloading test observations (Fig. 5). During superimposed dynamic sinusoidal indentation loading, a phase lag between the applied stress and the measured strain signal reveals viscoelastic behaviours. For an elastic solid, the resulting stress and strain should be totally in phase, while for a Newtonian viscous fluid there is a 90 º phase lag in strain with respect to the applied stress[37]. The tangent of the phase lag (tan δ) is the ratio of the storage modulus (*E'*) to the loss modulus (*E"*) as described below (Supplemental Fig. 3).

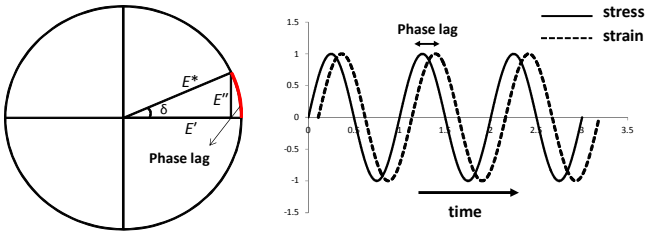

Supplemental Fig. 3
A diagram for the delayed stress-strain response in viscoelastic materials to calculate the tangent of the phase lag (tan δ).

$$\tan\delta = \frac{E''}{E'} \quad (2)$$

$$E' = \frac{S_e\sqrt{\pi}}{2\sqrt{A}} \quad (3)$$

$$S_e = \frac{\sigma_0}{\varepsilon_0}\cos\delta \quad (4)$$

where A is the projected contact area obtained by manual curve fitting of the slope at the onset of unloading following sinusoidal indentation, σ_0 is the stress amplitude, ε_0 is the strain amplitude, and δ is the phase lag (radian)[11]. A correction for elastic modulus determination can be made by equation (3) with the effective contact stiffness S_e defined as equation (4).

The delayed displacement during constant load (0 Hz) revealed the time-dependent creep behaviour of the samples. The elastic modulus can be calculated based on equation (1). Elastic contact stiffness (S) is determined as the slope of the unloading load versus displacement curve (Eq. 1), assuming that the unloading response is elastic. For a viscoelastic material, the onset of the unloading slope can exceed its contact stiffness because of the influence of creep deformation[38], thereby resulting in an overestimation of elastic modulus according to equation (1). A correction for elastic modulus determination can be made by replacing S (Eq. 1) with the effective contact stiffness S_e defined as[38, 39].

$$S_e = \left(\frac{1}{S} - \frac{\dot{h}_h}{\dot{P}_u}\right)^{-1} \quad (5)$$

where $\dot{h}_h > 0$ is the displacement rate at the end of the load-hold period immediately prior to unloading and $\dot{P}_u < 0$ is the unloading rate at the onset of unloading. The displacement rates were calculated by linear approximation fitting. We examined the displacement rate within 5 s prior to the onset of unloading and slope determination (Supplemental Fig. 4A).

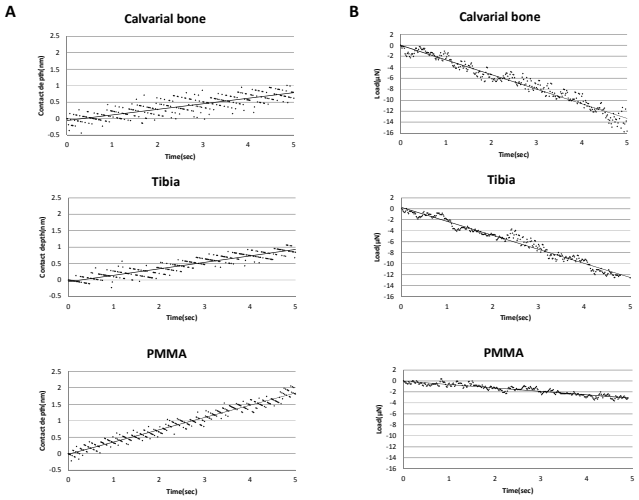

Supplemental Fig. 4
The linear approximation fits prior to the onset of unloading obtained from load-controlled (A) and displacement-controlled (B) indentations.

Displacement control

Force-displacement curves were recorded using a 20 nm/s loading rate to a maximum depth of 200 nm determined by the effective tip area function and the measurement range. A loading slope was followed by 60 s hold at 200 nm contact depth. During this period, the force decreased as expected due to stress relaxation associated with the visco- (and/or poro-) elastic response[15, 27]. The stress relaxation ratio (%) to maximum loading force was calculated. For viscoelastic materials at the onset of unloading, the slope can decrease its contact stiffness (S) because of stress relaxation[15], thereby underestimating the elastic modulus according to equation (1). An estimate of the purely elastic property (storage modulus),

however, can be determined via equation (1) by replacing *S* with the effective contact stiffness *Se* defined by the following equation[15].

$$S_{\mathrm{e}} = S + \frac{\dot{P}_h}{v_h} \qquad (6)$$

where $\dot{P}_h$ is the rate of relaxation of the force on the indenter immediately before indenter displacement and v_h is the displacement rate at beginning of indenter withdrawal. The relaxation rates were calculated by linear approximation fitting. We examined the relaxation rate within 5 s prior to commencement of unloading and associated slope determination (Supplemental Fig. 4B).

Statistical analysis

Three indentations were performed in the preliminary loading/partial unloading tests. At least five regions, each with five indentations, were evaluated using micro-Raman spectroscopy analyses and nanoindentation tests. The results are expressed as the mean ± standard deviation for each experiment. The normal distribution of each dataset was confirmed using the Kolmogorov–Smirnov test. The validity of the homogeneous variances assumption was investigated by Bartlett's test. Data were analyzed by ANOVA followed by a Tukey post-hoc tests. A *p*-value of less than 0.05 was considered significant.

Conclusion

Although time-dependent energy dissipation was reduced with increased bone mineralization, strain-rate stiffening may be more resistant to excessive deformation during the initial application of large stresses. Moreover, a nanoscale dimensional recovery process almost independent of viscoelasticity enables large force reduction during rapid strain application. This study also implies that the observed strain-rate stiffening and consequent dimensional recovery effects may be an underlying mechanism for the remarkable durability of mineralized tissues such as bone and teeth.

Acknowledgements

We thank Dr. Naoki Fujisawa and Dr. Ayako Mochizuki for the kind technical assistance for nanoindentation data analysis and bone sample preparations, respectively. This work was supported by a Grant-in-Aid for Scientific Research (B) and (C) from the Ministry of Education, Culture, Sports, Science and Technology of Japan. None of the authors have any conflicts of interest to declare.

Author contributions N.M. and Y.S. performed project planning, experimental work, data interpretation, and preparation of the manuscript. Wurihan, Y.K., and Y.T. performed experimental work. A.Y. participated in data analysis. M.V.S, K.M. and T.M. supervised the research and participated in project planning.

References

1. *L. Cristofolini, M. Viceconti, A. Cappello and A. Toni, J. Biomech., 1996, **29**, 525-535.*
2. *B. Ji and H. Gao, J. Mech. Phys. Solids., 2004, **52**, 1963-1990.*
3. *C. A. Pattin, W. E. Caler and D. R. Carter, J. Biomech., 1996, **29**, 69-79.*
4. *P. A. Janmey, M. E. McCormick, S. Rammensee, J. L. Leight, P. C. Georges and F. C. MacKintosh, Nat. Mater., 2007, **6**, 48-51.*
5. *W. A. Lam, O. Chaudhuri, A. Crow, K. D. Webster, T. D. Li, A. Kita, J. Huang and D. A. Fletcher, Nat. Mater., 2011, **10**, 61-66.*
6. *C. Storm, J. J. Pastore, F. C. MacKintosh, T. C. Lubensky and P. A. Janmey, Nature, 2005, **435**, 191-194.*
7. *S. H. Tung and S. R. Raghavan, Langmuir, 2008, **24**, 8405-8408.*
8. *K. Wang and D. Sun, J. Biomech., 2012, **45**, 1900-1908.*
9. *L. E. Bertassoni, J. P. R. Orgel, O. Antipova and M. V. Swain, Acta Biomaterialia, 2012, **8**, 2419-2433.*
10. *L. E. Bertassoni and M. V. Swain, J. Mech. Behav. Biomed. Mater., 2014, **38**, 91-104.*
11. *H. Isaksson, S. Nagao, M. Małkiewicz, P. Julkunen, R. Nowak and J. S. Jurvelin, J. Biomech., 2010, **43**, 2410-2417.*
12. *D. M. Ebenstein and L. A. Pruitt, Nano Today, 2006, **1**, 26-33.*
13. *O. Franke, M. Göken, M. A. Meyers, K. Durst and A. M. Hodge, MAT. SCI. ENG. C., 2011, **31**, 789-795.*
14. *N. Fujisawa and M. V. Swain, J. Mater. Res., 2008, **23**, 637-641.*
15. *Y. T. Cheng, W. Ni and C. M. Cheng, J. Mater. Res., 2005, **20**, 3061-3071.*
16. *V. T. Nayar, J. D. Weiland, C. S. Nelson and A. M. Hodge, J. Mech. Behav. Biomed. Mater., 2012, **7**, 60-68.*
17. *D. Felsenberg and S. Boonen, Clin. Ther., 2005, **27**, 1-11.*
18. *O. L. Katsamenis, H. M. H. Chong, O. G. Andriotis and P. J. Thurner, J. Mech. Behav. Biomed. Mater., 2012, **17**, 152-165.*
19. *D. Ulrich, T. Hildebrand, B. Van Rietbergen, R. Müller and P. Rüegsegger, Stud. Health Technol. Inform., 1997, **40**, 97-112.*
20. *S. H. Spiegelberg and G. H. McKinley, J. Non-Newton. Fluid., 1996, **67**, 49-76.*
21. *H. Lu, B. Wang, J. Ma, G. Huang and H. Viswanathan, Mechanics Time-Dependent Materials, 2003, **7**, 189-207.*
22. *S. S. Ionova-Martin, S. H. Do, H. D. Barth, M. Szadkowska, A. E. Porter, J. W. Ager Iii, J. W. Ager Jr, T. Alliston, C. Vaisse and R. O. Ritchie, Bone, 2010, **46**, 217-225.*
23. *Y. T. Chang, C. M. Chen, M. Y. Tu, H. L. Chen, S. Y. Chang, T. C. Tsai, Y. T. Wang and H. L. Hsiao, J. Mech. Behav. Biomed. Mater., 2011, **4**, 1412-1420.*
24. *T. Wenchang, P. Wenxiao and X. Mingyu, Int. J. Nonlinear. Mech., 2003, **38**, 645-650.*
25. *G. Boivin, Y. Bala, A. Doublier, D. Farlay, L. G. Ste-Marie, P. J. Meunier and P. D. Delmas, Bone, 2008, **43**, 532-538.*
26. *X. Wang, X. Shen, X. Li and C. Mauli Agrawal, Bone, 2002, **31**, 1-7.*
27. *M. L. Oyen, J. Mater. Res., 2008, **23**, 1307-1314.*
28. *R. E. Shadwick, J. Exp. Biol., 1999, **202**, 3305-3313.*
29. *B. Bar-On and H. Wagner, J. Struct. Biol., 2013, **183**, 149-164.*
30. *A. Shipov, P. Zaslansky, H. Riesemeier, G. Segev, A. Atkins and R. Shahar, J. Struct. Biol., 2013, **183**, 132-140.*

*31. T. Kawamoto, Arch. Histol. Cytol., 2003, **66**, 123-143.*
*32. A. Carden, R. M. Rajachar, M. D. Morris and D. H. Kohn, Calcif. Tissue Int., 2003, **72**, 166-175.*
*33. X. Bi, C. A. Patil, C. C. Lynch, G. M. Pharr, A. Mahadevan-Jansen and J. S. Nyman, J. Biomech., 2011, **44**, 297-303.*
*34. W. C. Oliver and G. M. Pharr, J. Mater. Res., 1992, **7**, 1564-1580.*
*35. W. C. Oliver and G. M. Pharr, J. Mater. Res., 2004, **19**, 3-20.*
*36. J. S. Field and M. V. Swain, J. Mater. Res., 1995, **10**, 101-112.*
*37. C. S. Sanctuary, H. W. A. Wiskott, J. Justiz, J. Botsis and U. C. Belser, J. Appl. Physiol., 2005, **99**, 2369-2378.*
*38. G. Feng and A. H. W. Ngan, J. Mater. Res., 2002, **17**, 660-668.*
*39. A. H. W. Ngan, H. T. Wang, B. Tang and K. Y. Sze, Int. J. Solids. Struct., 2005, **42**, 1831-1846.*

